Influence of gold on the reactivity behaviour of ceria nanorods in CO oxidation: Combining *operando* spectroscopies and DFT calculations

Marc Ziemba, Christian Hess*

Eduard Zintl Institute of Inorganic and Physical Chemistry, Technical University of Darmstadt, Alarich-Weiss-Str. 8, 64287 Darmstadt, Germany

*email: christian.hess@tu-darmstadt.de

Keywords

Ceria, gold, nanorods, nanocubes, CO oxidation, *operando* spectroscopy, Raman, UV-vis, density functional theory

Abstract

Au/CeO_2 catalysts are commonly used for low-temperature CO oxidation. While many studies focus on the properties of gold and their relevance for the activity, the influence of the support properties has received less attention. In this temperature-dependent study, we examine the relation between structure and activity for oxidation of CO over ceria nanorods (with/without gold), exhibiting $CeO_2(110)$ and $CeO_2(100)$ termination. Using ceria nanocubes with $CeO_2(100)$ termination as a reference enables us to extract facet-specific characteristics. To characterize the adsorbate and structural dynamics we employ *operando* Raman and UV-vis spectroscopy combined with density functional theory (DFT) calculations. Our results reveal the superiority of $CeO_2(110)$ over $CeO_2(100)$ facets for CO oxidation as a result of their lower defect formation energy. Our findings are supported by the observed dynamics of the surface peroxide, the subsurface oxygen, and the bulk reduction under *operando* conditions. The lower activity of the unloaded samples can be compensated by higher temperatures (>120 °C) allowing new insight into the role of gold for CO oxidation activity. Our study highlights the importance of the surface termination for a detailed mechanistic understanding of ceria-based catalysts.

Introduction

In previous studies Haruta et al. have demonstrated the suitability of a gold catalyst for low-temperature CO oxidation.[1] Later it was shown that the combination of gold with support materials, such as ceria, can further improve the catalytic activity.[2] The beneficial influence of ceria has been explained by the easy reducibility from Ce^{4+} to Ce^{3+}, the oxygen storage capacity, and its interaction with gas-phase molecules or the gold particles themselves.[3,4]

The oxidation of CO, in combination with the water–gas shift reaction, plays an important role in processes in which the purity of the H_2 stream is crucial, such as fuel cell applications.[5] Despite its relevance for low-temperature applications such as the latter process, as well as its importance as a prototype reaction in heterogeneous catalysis, the mechanism of the CO oxidation over ceria-supported gold catalysts is still hotly debated in the literature.

Previously, it has been shown that both the nature of the support (specific surface area, surface termination, particle size) and the nature of the gold particles is important.[6–9] While there have been a large number of studies dealing with the state of gold,[10–16] the changes in support properties that result from the presence of gold have attracted less attention. From density functional theory (DFT) studies is it known that gold particles can lower the defect

formation energy and the energy for oxygen activation.[13,17–19] On the other hand, previous experimental and theoretical work has demonstrated that the ceria surface termination affects properties such as the defect formation energy or the interaction with molecules from the gas phase.[9,20–23] For example, according to DFT studies, CO interacts more strongly with the CeO_2(110) and CeO_2(100) surfaces than with the CeO_2(111) surface.[24–26] In order to gain insights into the exact role of gold in CO oxidation and to assess its relevance in comparison to the surface termination, we have studied ceria samples with defined surface termination, with and without gold, at different reaction temperatures. On the basis of a Mars–van Krevelen type of mechanism, easy reducibility of the support is essential.[16,19,27] Therefore, in this publication we will focus on the two least-stable low-index CeO_2 surface terminations, i.e., CeO_2(100) and CeO_2(110), as they have been shown to possess lower defect formation energies than CeO_2(111).[21] We have used a combination of *operando* UV-vis and Raman spectroscopy and DFT calculations to elucidate the influence of the surface termination in the presence and absence of gold particles during CO oxidation.

Experimental Section

Catalyst Preparation. Ceria nanocrystals were prepared by hydrothermal synthesis, based on previous reports.[28,29] For ceria cubes and rods, first 79 ml of a NaOH solution (98%, Grüssing GmbH) was prepared (cubes: 6 M NaOH, rods: 9 M NaOH). In another beaker, the ceria precursor was dissolved in 11 ml of deionized water (electrical conductivity <3 $\mu S\ m^{-1}$). For the cubes, $Ce(NO_3)_3 \cdot 6H_2O$ (Alfa Aesar, 99.5%) served as the precursor, and for the rods, $CeCl_3 \cdot 7H_2O$ (Alfa Aesar, 99%). This solution was then added to the NaOH solution and stirred for 30 min. After that, the solution was poured into a PTFE autoclave (volume: 140 ml) and heated in an oven (heating rate: 1 °C/min) to the desired temperature (cubes: 180 °C, 18 h; rods: 140 °C, 48 h). After cooling to near room temperature, the resulting CeO_2 was centrifuged off and washed three times with deionized water before it was dried for at least 24 h at 85 °C in an oven.

Loading of the ceria nanoparticles with gold was carried out by means of electrolyte deposition. To this end, ceria samples were dispersed in a ratio of 1:150 in deionized water and the pH value was adjusted to 9 with a 0.1 M NaOH solution (98%, Grüssing GmbH). Subsequently, a 10^{-3} M $HAuCl_4 \cdot 3H_2O$ solution (Carl Roth, 99.9%) was prepared, also at pH 9. The $HAuCl_4 \cdot 3H_2O$ solution was then added to the ceria dispersion to obtain the desired loading of 0.5 wt% Au. After the addition, the pH value was checked again and adjusted to pH 9 if necessary. Then the mixture was heated for 2 h at 65 °C. After cooling it was placed in an

ultrasonic bath for 30 min. Finally, the residue was centrifuged and washed four times with deionized water before the product was dried at 85 °C for at least 24 h in an oven.

Catalyst Characterization

BET. N_2 adsorption at 77 K was conducted on a Surfer (Thermo Fisher Scientific). Before measurement, the sample was outgassed at 80 °C in high vacuum (10^{-6} bar) for 48 h. To determine the specific surface area, the N_2 adsorption curve was fitted to the BET (Brunauer–Emmett–Teller) model.[30] For the rods a specific surface area of 88 m^2/g and a pore volume of 0.22 cm^3/g were obtained. For the cubes, we found 32 m^2/g for the specific surface and 0.08 cm^3/g for the pore volume.

Transmission Electron Microscopy (TEM). The transmission electron microscope (JEOL JEM-2100F, Tokyo, Japan) used is equipped with a Schottky field emitter and operates at a nominal acceleration voltage of 200 kV. For preparation, the sample was dispersed in an ultrasonic bath for 30 s in ethanol and then placed on a carbon grid (Plano). When the sample was dry, the grid was coated with carbon (Bal-Tec MED010), to prevent charging by the electron beam.[31]

X-Ray Photoelectron Spectroscopy (XPS). XP spectra were recorded on an SSX 100 ESCA spectrometer (Surface Science Laboratories Inc.) employing a monochromatic Al Kα source with an energy of 9 kV (10 mA). The sample holder and the analyser were aligned at an angle of 55° to the horizontal. The X-ray beam was at an angle of 35° to the analyser horizontal and the sample was rotated 16° with respect to the X-ray beam. The resolution was 0.054 eV.

To ensure the comparability of the spectra, the u″ signal of the Ce 3d photoemission was shifted to the literature value of 916.7 eV for all spectra.[32] The spectra were deconvoluted by Gaussian–Lorentz functions (30/70 ratio), whereby the background was subtracted according to Shirley.[33] For further details, please refer to previous studies.[34]

Based on the XPS data, the amount of gold for the loaded rods was determined to be 0.3 wt% Au, and for the gold-loaded cubes, 0.6 wt% Au. In this context, the amount of gold is given in weight percentage directly at the surface, which is due to the penetration depth of the method. Contaminations caused by the synthesis, e.g. chlorine or nitrogen, can be excluded within the sensitivity of the XPS measurements.

ICP-OES. The weight percentage of gold was determined by ICP-OES, yielding a gold content of 0.2 wt% for the rods and of 0.18 wt% for the cubes.

***Operando* Spectroscopy.** The catalytic activity, *operando* Raman, and UV-vis spectra were measured using an experimental setup that has been described previously.[34–36] Briefly, for the

operando measurements about 20–25 mg of the sample was placed in a stainless-steel sample holder (8 mm in diameter, 0.5 mm deep). Raman spectra were recorded on an HL5R transmission spectrometer (Kaiser Optical) using a frequency-doubled Nd:YAG laser (Cobolt) for excitation at 532 nm (1 mW at sample). The spectral resolution was specified as 5 cm^{-1} and the stability of the band positions was better than 0.3 cm^{-1}. For the cubes an exposure time of 80 s with 5 accumulations was used, and for the rods, an exposure time of 250 s with 2 accumulations. For all measurements a cosmic ray filter and an auto new dark correction were used. This results in a total measuring time of about 1600 s for cubes and 2000 s for rods. All Raman spectra reported in this work were normalized to the highest intensity band, i.e., the F_{2g} band. Given F_{2g} positions were determined by curve fitting using Lorentz functions.

The UV-vis spectra were taken in diffuse reflection using an AvaSpec ULS2048 spectrometer (Avantes) equipped with a deuterium lamp and a halogen discharge lamp. The measuring time was 60 s, which is composed of an exposure time of 300 ms and 200 runs. As the white standard, magnesium oxide powder (MgO, Sigma Aldrich) was used, which shows no absorption between 170 nm and 1100 nm.

The sample temperature was determined by means of a Ni/Cr-Ni thermocouple (type K), which was located at the sample holder close to the sample. Sample temperatures deviated by a maximum of 2 °C from the set temperatures. The temperature difference for the unloaded and gold-loaded samples (121 °C and 134 °C) corresponds to differences in the heat of reaction, as the CO oxidation is a highly exothermic reaction.

The gases CO (99.997%, Air Liquide), O_2 (99.999%, Westfalen), and argon (99.996%, Westfalen) were dosed by digital mass flow controllers (MFCs, Bronkhorst). The total flow was always 100 ml/min. To analyse the gas phase and its composition, a Fourier transform infrared (FTIR) spectrometer (Tensor 20, Bruker) was installed at the outlet of the cell. The resolution was 4 cm^{-1}, and the measurement time was 1 min, in which 125 spectra were accumulated. Using calibration curves, the concentrations of CO and CO_2 can be calculated to determine the CO conversion. This catalytic activity is obtained as the ratio of the amount of CO_2, as measured by FTIR at the outlet of the cell, and the amount of CO dosed (2 ml/min), which corresponds to the conversion of CO to CO_2.

DFT Calculations. The employed approach and procedures have been described previously.[9,37] Briefly, spin-polarized DFT calculations were performed using the Vienna Ab initio Simulation Package (VASP, Version 5.3.5, https://www.vasp.at/). For all calculations the DFT+U approach[38] with the generalized gradient-corrected approximation of Perdew, Burke and Ernzerhof (PBE) was employed,[39] and for the U_{eff} of the Ce 4f orbital parameter 4.5 eV

(PBE + U / 4.5 eV) was used. Only valence electrons with a plane-wave cutoff of 400 eV were considered. The pseudopotentials used originated from VASP version 5.4 and the Kohn–Sham equations were solved using the projector augmented wave (PAW) method. As the lattice constant for ceria we used 5.484 Å.[37] For all relaxations of the structures, the convergence criterion was set to 0.01 eV/Å, which describes the maximum force acting on an atom. The total energy for a self-consistent loop was converged up to 10^{-6} eV.

The supercell used for CeO_2(110) consists of seven atomic layers, the lowest of which is fixed. At the top and bottom of the cell, a vacuum layer of at least 10 Å was added. The choice of the number of atomic layers was based on the convergence of the surface energy. The relaxation energy plot for the CeO_2(110) facet is shown in Figure S1. For the calculations, unit cells with (1×1), (2×1), and (2×2) periodicities were used. The sampling of the Brillouin zone was realized according to the periodicity with a (6×4×1), (3×4×1), or (3×2×1) Monkhorst–Pack grid,[40] which correspond to the same k-point density in terms of the periodicity. To model the gold/ceria structures gold atoms were deposited on CeO_2(110) or CeO_{2-x}(110) structures, using previous theoretical studies as an orientation for modelling the structures.[41–43] Furthermore, a Bader charge analysis was performed for the gold atoms (see Table S2), which shows that when gold interacts with the oxidized ceria surface, a charge transfer to cerium takes place resulting in positively charged gold atoms. By interaction of gold with a reduced ceria surface this is reversed leading to negatively charged gold atoms, consistent with previous DFT studies.[42,44]

The vibrational frequencies were calculated using density functional perturbation theory (DFPT), which is implemented in the VASP code. The calculation of Raman intensities has been described previously.[37]

Results

Catalyst Characterization. The prepared nanoparticles were characterized by BET, TEM (see Figure 1), XPS (see Figures S2 and S3) and ICP-OES. The TEM images for ceria rods and ceria cubes, shown as Figure 1A and 1B, respectively, indicate the characteristic surface terminations of the particles, based on the spacing of the lattice planes indicated by the white arrows. The rods exhibit two different lattice plane distances, i.e., 0.27 nm and 0.19 nm, whereas the cubes are characterized by a single lattice plane distance of 0.27 nm. A distance of 0.27 nm can be assigned to a CeO_2(100) termination and a distance of 0.19 nm to a CeO_2(110) termination, in agreement with the literature.[28,29] Using the cubes as a reference for CeO_2(100) throughout our study allows us to assign effects observed for the rods to a specific facet, i.e., either CeO_2(110)

or CeO_2(100). While we focus on the rods here, the corresponding results for the cubes are shown in the Supporting Information.

Analysis by XPS reveals a Ce^{3+} content of 15% for the bare ceria rods and 38% for the gold-loaded rods. The increase of the Ce^{3+} content with the gold loading can be explained by a charge transfer from gold to the oxidized ceria resulting in $Au^{\delta+}$ and Ce^{3+} (see Figure S10 and Table S2), consistent with previous DFT+U calculations.[13,42,45] In the Au 4f photoemission of the gold-loaded rods (see Figure S4), there are two components, located at 84.2 and 87.5 eV, originating from metallic and cationic gold, respectively. Although in previous studies Au^{3+} on CeO_2(111) has been observed by the adsorption of Au into cerium defects,[46] earlier studies for CeO_2(110) and CeO_2(100) have shown the absence of Au^{3+}.[18] Calculations from this study show that the presence of Au^{3+} cannot be excluded (see SI), because for the doped structures (Structures H and I, Table S2) the Bader charge is much higher than for the adsorbed gold species (e.g. Structures F and G, Table S2). However, theoretical studies have demonstrated that the adsorption of gold into cerium vacancies is only favored under extremely O-rich conditions compared to adsorption into oxygen defects,[47] because the formation of a cerium vacancy is a highly endothermic process, which is also in line with our calculations for the CeO_2(110) facet (see SI, Table S1). Based on these previously reported results we propose that the 87.5 eV component originates from $Au^{\delta+}$, despite the high binding energy. In this context it should be mentioned that signals at such high binding energies have previously been assigned to Au^{3+}, but this was based on gold salts and other gold reference compounds,[48] rather than supported gold particles.

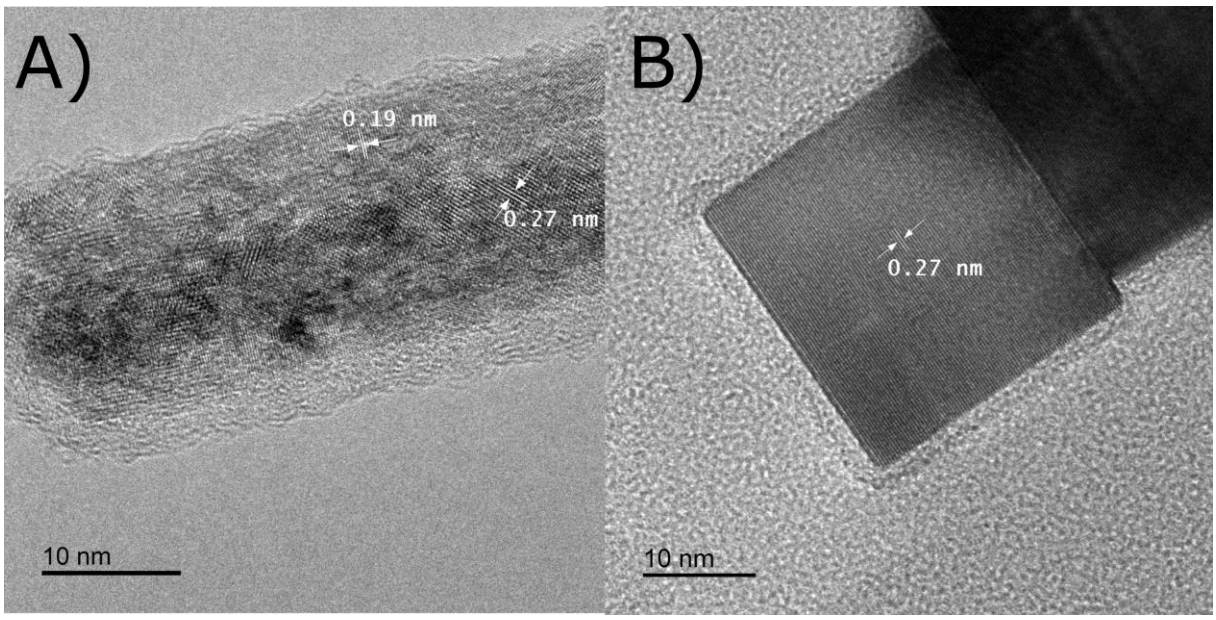

Figure 1: TEM images of the synthesized ceria nanostructures: **A)** ceria rod, and **B)** ceria cube. The white arrows indicate the distance between lattice planes in the direction of the particle surface.

Catalytic Activity. Figure 2 depicts the catalytic activity during CO oxidation (2% CO / 25% O_2 / Ar; 100 ml/min) over bare CeO_2 nanorods and 0.3 wt% Au/CeO_2 nanorods at two temperatures. Bare rods were measured at 45 °C and 121 °C, and gold-loaded rods at 45 °C and 134 °C. Prior to and after reaction, samples were exposed to oxidative conditions (25% O_2 / Ar; 100 ml/min). These measurements are also the basis of the *operando* measurements discussed below.

As can be seen in Figure 2, at 45 °C, the sample without gold loading shows no CO conversion, whereas the gold-loaded sample shows a conversion of 0.4%. At the higher temperature, the unloaded sample shows a small conversion of about 0.2% too. In comparison, the gold-loaded sample shows a conversion of 19.6% at 134 °C. Thus, depending on the conditions, both samples may show CO oxidation activity. Obviously, the presence of gold lowers the reaction barrier and/or assumes a stabilizing role of reaction intermediates. Regarding the reaction barrier, previous theoretical studies for CeO_2(100) have shown that Au_3 or larger gold clusters on CeO_2(100) can reduce the defect formation energy in contrast to unloaded CeO_2(100).[14] Our results for Au_1 on CeO_2(110) (see Table S2) also show that such small clusters do not reduce the defect formation energy as compared to unloaded ceria with CeO_2(110) facets. For this reason, we suggest that in case of the CeO_2(110) facet the presence of larger gold clusters is responsible for lowering the defect formation energy. However, the absence of gold can be compensated by higher temperatures, as will be discussed below in more detail in the context of the *operando* data.

A similar activity behaviour is also observed for the cubes (see Figure S5). However, it is noticeable that the CO conversion at 45 °C is lower than that of the rods, despite the higher gold loading at the surface (0.6 wt%). Based on this comparison, we attribute the higher activity of the rods to the CeO_2(110) facet. Interestingly, at higher temperatures, this difference is compensated again and similar conversions are observed for both the unloaded and gold-loaded samples at 45 °C. The catalytic activities for CO oxidation over unloaded and gold-loaded rods and cubes are summarized in Table 1.

Table 1: Catalytic activities for the conversion of CO to CO_2 during CO oxidation of the unloaded and gold-loaded rods and cubes. The catalytic activity was measured after at least 1 h

under reaction conditions ($CO/O_2/Ar$). Activities were determined at 45 °C and at an elevated temperature, i.e., at 121 °C for the unloaded samples and 134 °C for the gold-loaded samples.

Sample	**Activity at 45 °C**	**Activity at >120 °C**
CeO_2 rods	0.0	0.2
Au/CeO_2 rods	0.4	19.6
CeO_2 cubes	0.0	0.2
Au/CeO_2 cubes	0.1	20.1

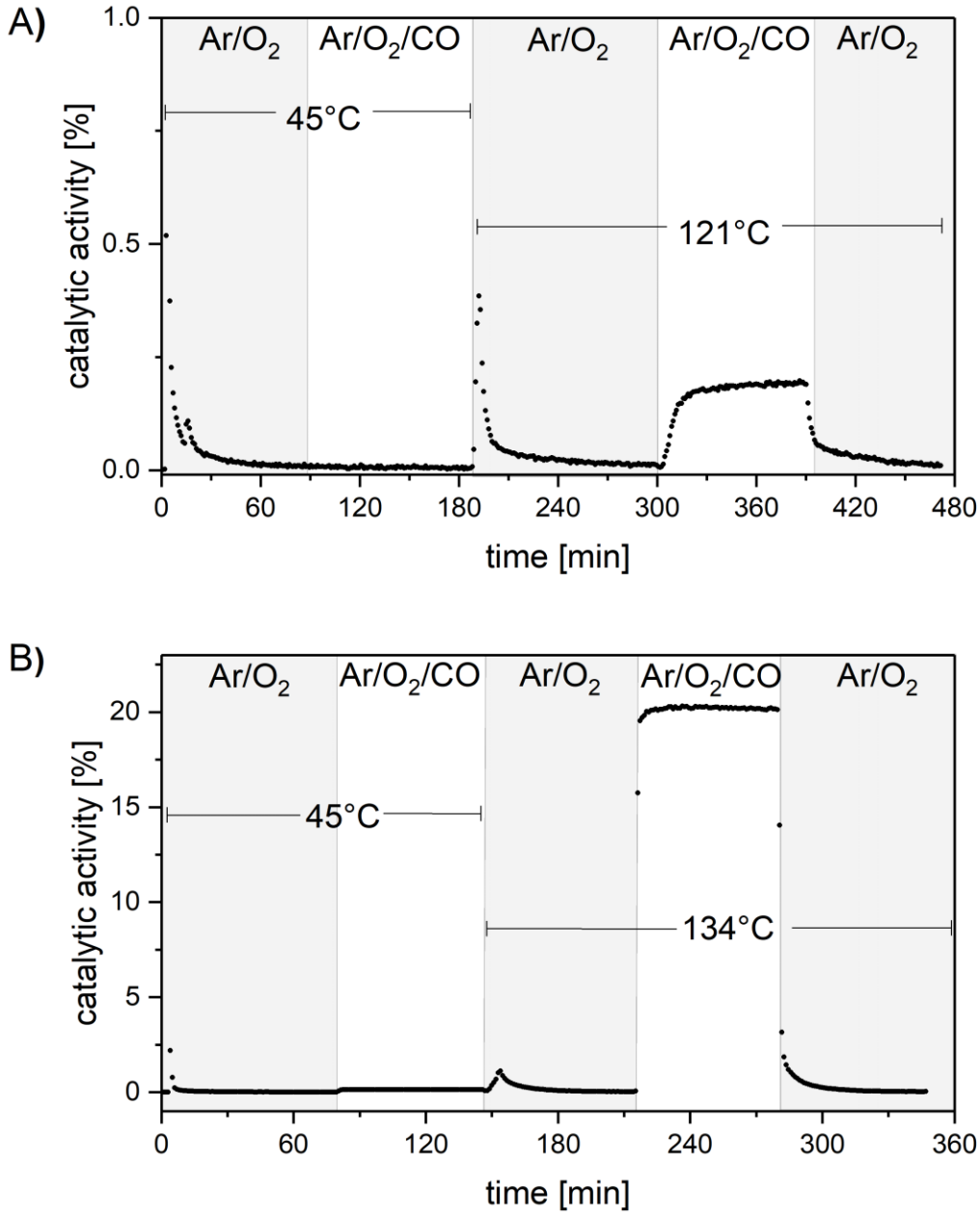

Figure 2: Catalytic activity during CO oxidation over **A)** CeO_2 nanorods at 45 °C and 121 °C, and **B)** 0.3 wt% Au/CeO_2 nanorods at 45 °C and 134 °C. The samples were exposed to a CO/O_2/Ar stream (2% CO/25% O_2/Ar; 100 ml/min) under reaction conditions and to an O_2/Ar stream (25% O_2/Ar; 100 ml/ min) prior to and after reaction conditions, respectively.

***Operando* UV-vis Spectroscopy.** Changes of the electronic structure under reaction conditions can be detected using *operando* UV-vis spectroscopy. To this end, Figure 3 depicts *operando* UV-vis spectra of bare ceria rods and gold-loaded rods. The spectra shown at the bottom (dashed lines) represent the measurements of the unloaded sample and the spectra at the top

(solid lines) those of the loaded sample. Both samples exhibit strong absorption in the UV range, attributable to O 2p (occupied) → Ce 4f (unoccupied) interband and f → d transitions.[49,50] Comparison of the spectra of the two samples at 45 °C in $CO/O_2/Ar$ shows that the presence of gold leads to increased absorption in the visible range (450–900 nm). This behaviour is attributed mainly to a charge transfer from Ce^{3+} to Ce^{4+},[50,51] while absorption due to gold surface plasmons cannot be ruled out.[52] Plasmon-induced absorption appears to be more important for the Au/CeO_2 cubes (see Figure S6), which show a stronger absorption in the visible wavelength region despite the lower Ce^{3+} content of 28 % (XPS) (compare –log(*R*) at 570 nm (45 °C in O_2/Ar); rods: 0.17, cubes: 0.32). Interestingly, under reaction conditions at 45 °C, the gold-loaded rods exhibit an absorption band between 450 nm and 550 nm, which is barely noticeable for the other samples. To the best of our knowledge, this band has previously been associated with adsorbed oxygen species,[53] but has not been discussed in more detail in the literature. Based on its correlation with the appearance of the peroxide Raman band at 829 cm^{-1} discussed below (see Figure 4B), it is tentatively assigned to peroxides adsorbed on the ceria surface.

When the feed is switched from reactive conditions at 45 °C to O_2/Ar flow at higher temperature, an increase in absorption is observed between 400 nm and 500 nm, which is assigned to a temperature-induced decrease of the band gap, in agreement with the literature.[54] Exposure to reaction conditions leads to a further increase in visible absorption (green lines), which, however, shows a profile different to that at 45 °C (red lines). The absorption increase may originate from an agglomeration of gold particles, as previously described in the literature,[10,52] and/or from a reduction of the support, as will be discussed below in the context of the *operando* Raman data. In contrast to the $CeO_2(111)$ facet, an irreversible adsorption of gold into oxygen vacancies can be excluded on the $CeO_2(110)$ facet, since this process is reversible on the $CeO_2(110)$ facet due to the more open surface.[55] However, on the $CeO_2(100)$ facet, such a process would be conceivable. Finally, switching the feed to O_2/Ar leads to a small decrease in absorption but no regeneration of the initial state.

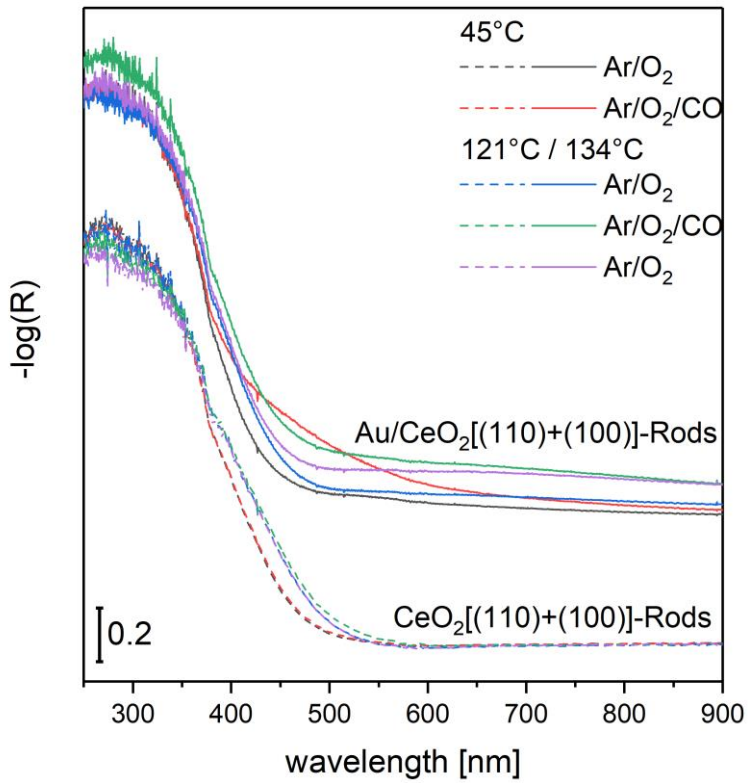

Figure 3: *Operando* UV-vis spectra of bare ceria rods (at the bottom, dashed lines) and gold-loaded rods (at the top, solid lines). The spectra were recorded at the temperatures indicated, at a total flow rate of 100 ml/min and feed compositions of 2% CO/25% O_2/Ar and 25% O_2/Ar for reactive and oxidative conditions, respectively. Spectra of the gold-loaded samples are offset for clarity.

***Operando* Raman Spectroscopy.** Figure 4 depicts the low-wavenumber region of the *operando* Raman spectra of bare ceria rods (Figure 4A) and gold-loaded rods (Figure 4B). As discussed in the following, this region contains features characteristic of solid-state phonons and adsorbate-related vibrations. Note that the high intensity F_{2g} peak at around 450 cm^{-1} is cut off to allow an enlarged view of the other features. In all spectra, the 2TA and the 2LO overtones are observed at 254 and 1170 cm^{-1}, and defect-related bands at 540 and 590 cm^{-1}.[37] The Raman band located at 829 cm^{-1} originates from peroxides adsorbed on the surface.[22] For the gold-loaded rods at 45 °C, the 829 cm^{-1} band contains a shoulder at 879 cm^{-1}, which is characteristic of the presence of peroxides at higher coverage, in agreement with our previous DFT calculations.[22]

Interestingly, the gold-loaded sample shows greater dynamics among the defect-related bands and a higher intensity in the peroxide region, both of which can be attributed to a reduction of the defect formation energy with gold loading, consistent with the literature.[13,14,17,18] Besides, the spectra of the loaded rods recorded at 45 °C in $CO/O_2/Ar$ (red line in Figure 4B) show an additional Raman feature at 354 cm^{-1}, which can be assigned to a deformation mode of peroxides on the ceria surface, as confirmed by DFT calculations (Figure S7), and in agreement with previous experimental observations on $CeO_2(111)$, which, however, did not clarify the symmetry of this vibration.[56] Note that, owing to its overlap with other bands, the peroxide feature at 354 cm^{-1} is only observed at higher peroxide coverages. For the cubes, this band is much less pronounced owing to the lower peroxide coverage, as inferred from the lower intensity of the 829 cm^{-1} peroxide band (see Figure S8).

Regarding adsorbate-related features, for the gold-loaded sample at 45 °C, a band at 1647 cm^{-1} is observed (see Figure 4B), the intensity of which increases under reaction conditions. Based on previous DFT calculations, this band can be assigned to a C=O vibration of carbonates on the surface.[35] At higher temperatures, this band is not detected.

Figure 5 covers the corresponding high-wavenumber region of the *operando* Raman spectra of bare ceria rods (shown at the bottom) and gold-loaded rods (shown at the top). In the spectra of both samples, bands appear at 2846 cm^{-1} and 2935 cm^{-1}, which can be attributed to C–H stretching vibrations of formates.[57] Note that, in the case of the gold-loaded sample, these bands lose intensity at higher temperature (see blue solid line) and are no longer observed under and after reaction conditions (see green and purple solid lines). Together with the temperature-dependent activity behaviour (see Figure 2), this observation may indicate a change in the reaction mechanism at higher conversions. As discussed previously for Pt/CeO_2 systems, at higher temperatures (98 °C) new reaction pathways via formates and/or a direct route may open up.[58] For a reaction via formates, the presence of hydroxides or water is essential. In fact, as shown in Figure 5, the presence of hydroxides in the range 3000–3800 cm^{-1} can be confirmed by the *operando* spectra. However, this aspect will be discussed in more detail below.

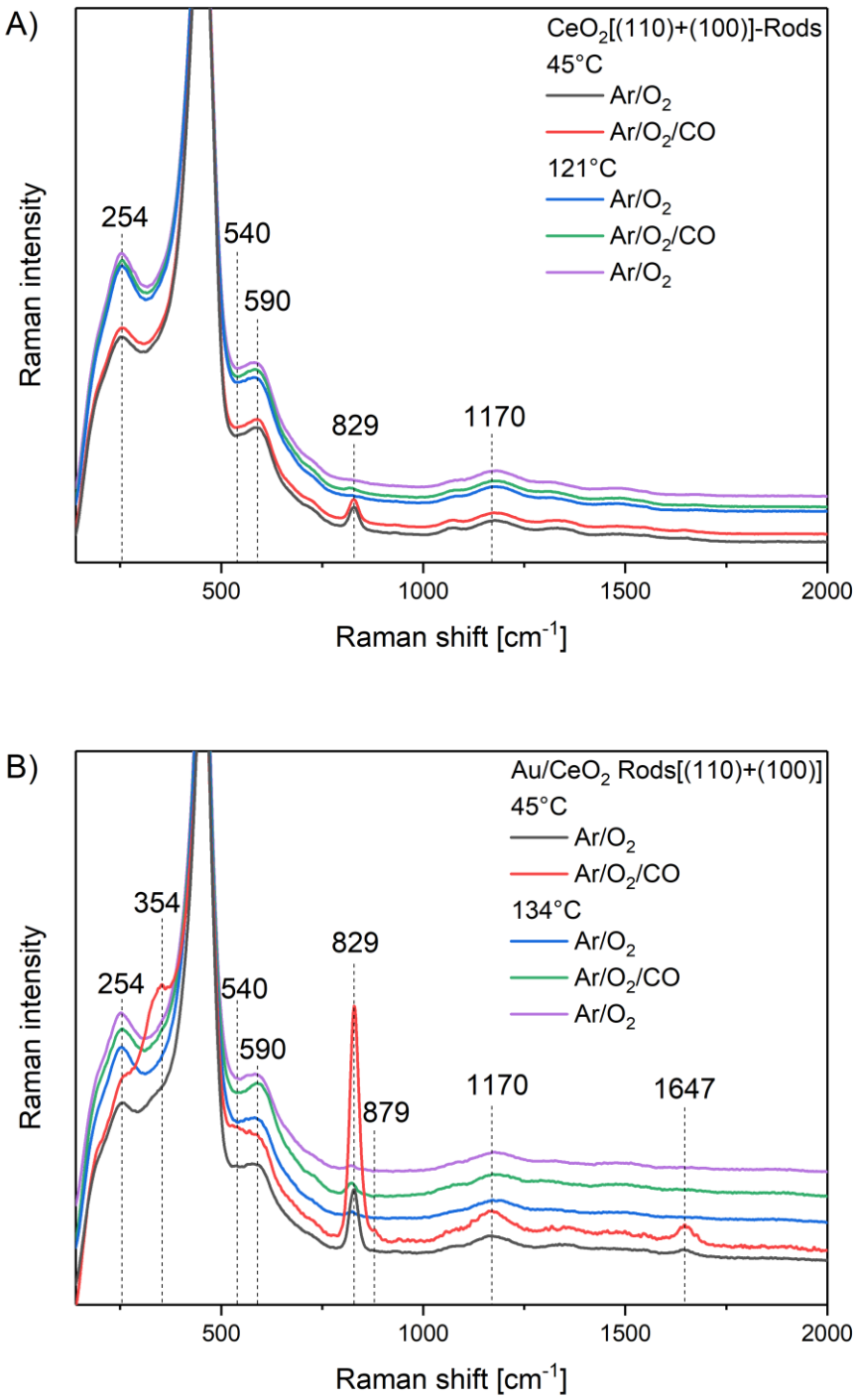

Figure 4: *Operando* 532 nm Raman spectra of **A)** bare ceria rods, and **B)** gold-loaded rods. The spectra were recorded at the temperatures indicated, at a total flow rate of 100 ml/min and feed compositions of 2% CO/25% O_2/Ar and 25% O_2/Ar for reactive and oxidative conditions, respectively. The high intensity F_{2g} peak at around 450 cm^{-1} is cut off to allow an enlarged view of the other features. Spectra are offset for clarity.

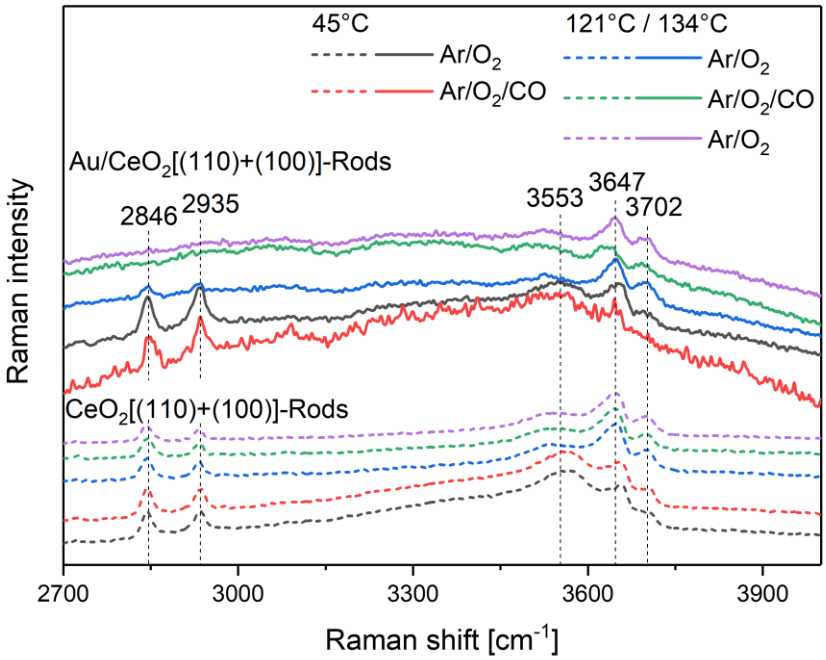

Figure 5: *Operando* 532 nm Raman spectra of the high-wavenumber region of bare ceria rods (at the bottom, dashed lines) and gold-loaded rods (at the top, solid lines). The spectra were recorded at the temperatures indicated, at a total flow rate of 100 ml/min and feed compositions of 2% CO/25% O_2/Ar and 25% O_2/Ar for reactive and oxidative conditions, respectively. Spectra are offset for clarity.

Dynamical behaviour under working conditions

Figure 6 depicts a summary of distinct *operando* Raman and UV-vis results of bare ceria rods (see Figure 6A) and rods loaded with 0.3 wt% Au (see Figure 6B). In particular, we will address the dynamical behaviour of the peroxide intensity, the Raman F_{2g} band position, and the absorption at 570 nm, in comparison to the simultaneously recorded catalytic activity. In the following, first the surface dynamics based on the peroxides, then the subsurface region as monitored by the F_{2g} band, and finally the visible absorption behaviour will be discussed.

As shown previously, peroxides can be regarded as an indicator for the presence of surface defects, as peroxide formation occurs via adsorption of gas-phase oxygen into a two-electron surface defect.[22,59] In fact, switching from oxidative (O_2/Ar) to reactive (CO/O_2/Ar) conditions at 45 °C leads to a strong increase of the peroxide intensity at 829 cm^{-1} of the gold loaded samples, as a result of the reduction by CO (see also Figure S11), whereas the bare ceria samples show no noticeable changes. However, as apparent from Figures 6 and S11, there are significant differences in the absolute intensity of the peroxide band. The gold-loaded samples

exhibit higher peroxide intensity than the bare samples, and the rods show a significantly higher intensity than the cubes. At higher temperature the peroxide bands decrease, as their formation is no longer preferred thermodynamically, as shown in our previous Raman and DFT studies.[22]

Regarding the Raman F_{2g} band, which represents the degree of reduction in the subsurface region,[36] loading ceria rods with gold induces a blue-shift of 4 cm^{-1} (see Figure 6), strongly suggesting that gold adsorbs into oxygen defects. The observed F_{2g} blue-shift can be rationalized by an electron transfer from Ce^{3+} to gold, which results in Ce^{4+} formation. As a consequence, the lattice is contracted because of the smaller ionic radius of Ce^{4+}, which is known to be accompanied by F_{2g} mode stiffening.[37] When exposed to O_2/Ar and reactive conditions at 45 °C, both rods and Au-loaded rods show an overall F_{2g} blue-shift, indicating sample oxidation. In the case of the cubes (see Figure S11), a contrary behaviour, i.e., a red-shift, is observed, which is attributed to temperature-induced mode softening.[60,61] This difference in behaviour between rods and cubes can be rationalized by the higher defect content of the rods (see XPS results in Supporting Information) and by the lower defect formation energy at the CeO_2(110) facet facilitating further oxidation in comparison to the cubes.

When exposed to higher temperature and oxidizing atmosphere, both rod-based samples undergo a further red-shift, which originates from the temperature effect (discussed above) and the (partial) removal of adsorbates, i.e., peroxides and CO, from the surface. The observed F_{2g} red-shift is significantly stronger for the gold-loaded cubes (2.8 cm^{-1}) than for the gold-loaded rods (0.5 cm^{-1}), as shown by Figures 6 and S11. This behaviour underlines the higher defect concentration of the rods indicated by the XPS measurements. If the feed is switched to reaction conditions at higher temperatures, the two rod samples show opposite behaviour regarding the F_{2g} position, i.e., the bare rods exhibit a blue-shift whereas the gold-loaded rods show a red-shift. This behaviour originates from the significantly higher CO conversion of the gold-loaded sample leading to reduction of ceria in the subsurface, since under these conditions the regeneration of the support is slower than the reduction by CO oxidation. Upon subsequent switching to oxidizing conditions, the gold-loaded sample is re-oxidized, while the bare-rod sample undergoes only little change, as this sample has already been re-oxidized under reaction conditions. This is different for the loaded and unloaded cubes (see Figure S11), which do not show noticeable F_{2g} shifts on switching between oxidative and reactive conditions, thus underlining the importance of the surface facet. In this context we note that the presence of two facets present in rods, i.e., (110) and (100), may mutually influence each other leading to a variation of properties from the isolated facets.

In the following, the change in absorption at 570 nm will be discussed. As can be seen in Figure 6, the gold-loaded sample shows an increase in absorption under reaction conditions at both temperatures, which may originate from a reduction of the material and/or sintering of gold particles, as suggested on the basis of long-term studies.[52] The observed increase in absorption is not completely reversible, which would be consistent with agglomeration of gold atoms, ceria reduction and/or irreversible gold adsorption into oxygen defects on CeO_2(100) at high conversion. For the gold-loaded cubes (see Figure S11) a similar behaviour is observed, but there is no decrease in absorption after switching to oxidative conditions, indicating a larger contribution of gold agglomeration and irreversible gold adsorption into oxygen defects on CeO_2(100). Regarding the latter explanation it should be noted that cubes possess a smaller defect concentration than rods (see above) and they contain only CeO_2(100) facets in contrast to the rods. In contrast, the unloaded rod samples show only slight reversible changes in 570 nm absorption under reaction conditions at elevated temperature from reaction induced reduction, whereas for bare cubes no changes are observed (see Figure S11), which can be related to the absence of the CeO_2(110) facet. Note that for the bare rods, the blue-shift of the Raman F_{2g} band points to an opposite oxidation behaviour in the subsurface region (see Figure 6A). This apparent contradiction can be resolved by taking into account the different penetration depths of the two methods, which monitor either the subsurface (Raman F_{2g}) or the bulk (UV-vis), thus implying oxygen diffusion from the bulk to the subsurface region in the case of the bare rods.

In this final section, we would like to discuss the apparently different findings regarding the Ce^{3+} contributions of the gold-loaded rods obtained by XPS (see Figure S3) and Raman (see Figure 6B). This can be explained by the penetration depths of the two methods, i.e., Raman probes the subsurface region[36] whereas XPS samples the surface region. Thus, gold adsorbed into the pores of ceria rods, causing the observed F_{2g} blue-shift, is not accessible by XPS. In contrast, such a F_{2g} blue-shift is absent for the cubes. This behaviour can be explained by taking into account the BET results, which show that the rods possess a significantly higher pore volume than the cubes.

Summarizing, our results show that the choice of the surface termination results in different structural dynamics of the surface, subsurface, and bulk. Based on these observations it is possible to obtain a more detailed understanding of the role of the support in Au/CeO_2 catalysts. In the following, we will discuss the implications of our findings regarding the mechanism of CO oxidation.

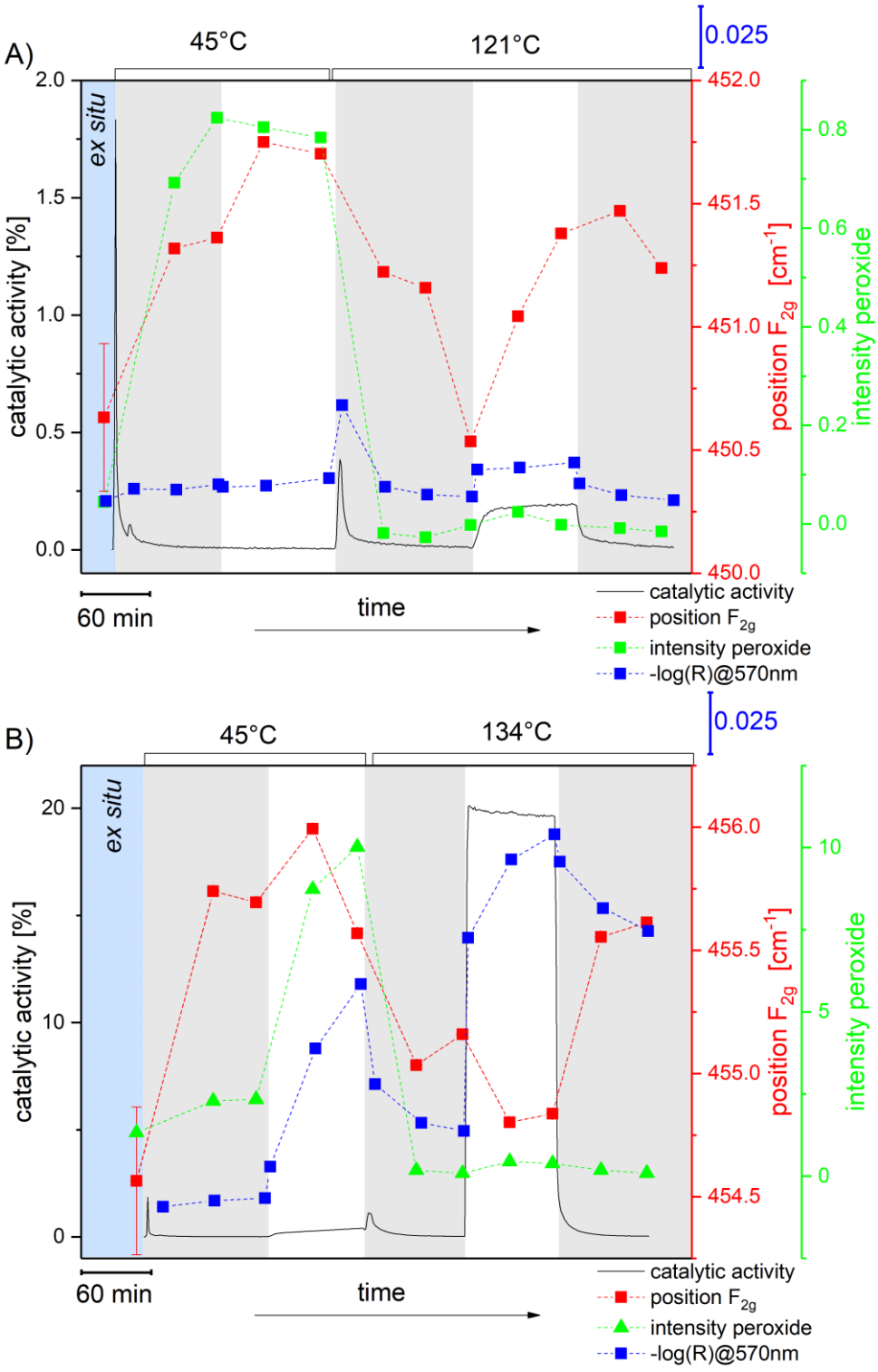

Figure 6: Summary of *operando* Raman and UV-vis results for **A)** bare ceria rods and **B)** 0.3 wt% Au/CeO_2 rods during CO oxidation (2% CO/25% O_2/Ar) at a total flow rate of 100 ml/min at the temperatures indicated. As in Figure 2, reaction conditions correspond to white areas, and oxidative conditions (25% O_2/Ar) to grey areas. The measurement error for

the F_{2g} position is indicated as an example for the *ex situ* measurement but applies to all F_{2g} data points.

Insight into the Reaction Mechanism

As demonstrated above, rods exposing CeO_2(110) and CeO_2(100) facets and cubes exposing CeO_2(100) facets can be active in CO oxidation with or without gold loading, but the presence of gold allows milder reaction conditions. The main findings are summarized in Figure 7 for the lower temperature, showing that bare ceria is not active and only CO adsorption and carbonate formation occurs. If gold is present, the sample becomes active for CO oxidation, as the presence of gold lowers the defect formation energy, making more surface oxygen available for reaction.[14,19] Furthermore, a coordinating role of gold on reaction intermediates may be conceivable, since the adsorption of CO (no carbonate formation) on deposited gold on oxidized ceria is preferred over the bare support (see Table S3). In fact, the identification of CO-Au^+-$O_{lattice}$ as an active site has already been demonstrated in our previous studies on Au/CeO_2(111) catalysts using a combination of DRIFTS and DFT calculations.[62] At higher temperatures, a different situation arises, as now both the bare support and the gold-loaded sample are active, owing to the fact that surface oxygen that is not located in the neighbourhood of gold is also available for CO_2 formation (see Figure 7). This behaviour can be explained by the thermally induced compensation of differences in the energy barrier for the formation of oxygen vacancies.

The importance of the defect formation energy for the catalytic activity is demonstrated by considering two different surface terminations. Generally, the rods show a higher activity at low temperatures than the cubes, consistent with the trends in the defect formation energies[21] (CeO_2(100): 1.392 eV;[22] CeO_2(110): 1.329 eV (see Table S1)), which are lower for CeO_2(110) present only at the rods. At higher temperatures, however, the activities are almost the same, owing to the loss of importance of the differences in defect formation energy.

Another aspect that may play a role regarding the activity at lower temperatures is the adsorption of peroxides. DFT calculations show that on all ceria facets the adsorption of O_2 is preferred over CO if CO adsorbs as an isolated molecule (i.e., without carbonate formation). Importantly, as shown by the activity profiles and peroxide intensity (see Figure 6), increasing peroxide formation at high coverages may impede CO oxidation, as indicated by the strong

peroxide signal during reaction conditions at 45 °C. While peroxides have been shown to participate in CO oxidation,[63,64] stable peroxide formation is indicative of an oxygen-deficient surface, which inhibits the formation of carboxylates/carbonates. Thus, the formation of CO_2 is expected to be more favourable under conditions where peroxide formation by O_2 adsorption is thermodynamically no longer preferred, e.g. at higher temperatures (> 120°C), at which peroxide dissociation is facilitated, thereby healing a second oxygen defect. Therefore, under these conditions, between steps 4 and 1 in Figure 7, dissociation of peroxide may take place, leading to adsorption of the outer oxygen atom into an adjacent oxygen vacancy (not shown) or a direct removal of the very reactive outer oxygen atom by CO, as shown in previous theoretical studies.[65]

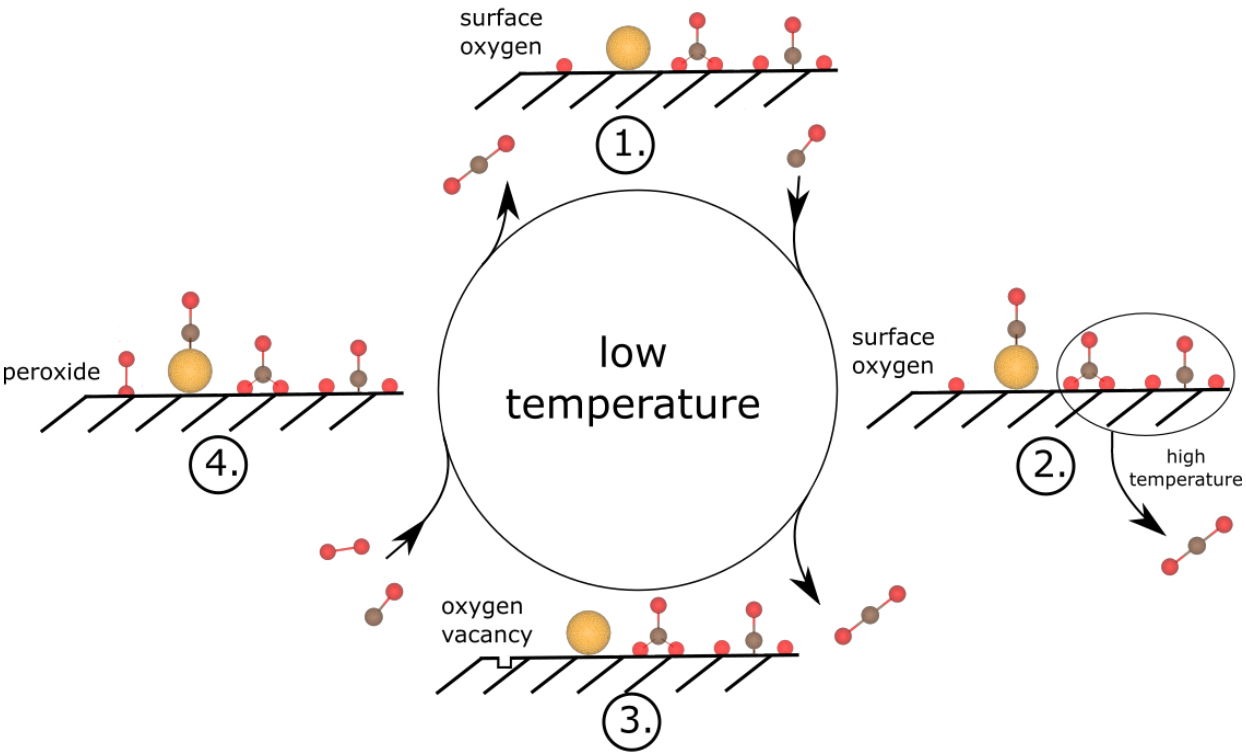

Figure 7: Reaction pathways for CO oxidation over bare CeO_2 and Au/CeO_2 catalysts at low temperature. For details see text.

In the following, we will discuss the role of carbonates, which were observed for the gold-loaded rods during reaction conditions (45 °C) (see Figure 4), and that of formates, which are present in all samples and disappear from the gold-loaded rods during reaction conditions at 134 °C (see Figure 5). For the cubes, no carbonates are observed, but their absence may result from the stronger absorption and therefore lower Raman sensitivity of the gold-loaded cube sample (see Figure S8). It has previously been shown in the literature for cobalt-doped ceria

systems that a carbonate-mediated mechanism may be feasible.[66] We may thus propose that at 45 °C CO adsorbs as carbonate without any CO conversion, consistent with theoretical results for CeO_2(110) and CeO_2(100) surfaces, demonstrating that carbonate formation is a strongly exothermic process.[23–25,67] In contrast, for the CeO_2(111) surface, no stable carbonate formation has been reported in the literature, which can be rationalized by the larger space between the surface oxygen atoms at the CeO_2(111) surface preventing carbonate formation without large surface reconstruction. As a consequence, the adsorption of carbonates at low temperatures negatively affects the activity, because active sites are blocked and carbonate adsorption is several times stronger than that of an isolated CO molecule.[25] Similarly, for CeO_2(111), the formation of hydrogencarbonates has been shown to inhibit CO oxidation by site blocking.[62,68] The situation is different at higher temperatures, at which the absence of the band at 1647 cm^{-1} may be explained by the formation of CO_2 via carbonates (indicated in Figure 7), leaving an oxygen vacancy. In addition, the resulting higher oxygen defect concentration at higher temperatures may inhibit the renewed formation of carbonates, since less surface oxygen is available for carbonate formation. Formates are characterized in this study by their C–H stretching bands at 2846 and 2935 cm^{-1} (see Figure 5).[69] In contrast to the bare rods, for the gold-loaded rods the C–H bands disappear at the higher temperature. Our results imply that the energy barrier for formate desorption is reduced for gold-loaded samples, leading to the disappearance of the bands without any indication of intermediates. In the course of this desorption process gold may play a major role, as gold can promote the proton transfer from formate species to surface oxygen at higher temperatures, resulting in the formation of hydroxide. The transfer of a second proton may then lead to water desorption accompanied by oxygen vacancy creation. Thus, we propose that formates are only spectator species for CO_2 formation, the desorption of which is facilitated in the presence of gold. As explained above, for the cubes no precise statements regarding formates can be made.

Conclusions

In this study, we demonstrate the importance of the defect formation energy for CO oxidation over Au/CeO_2 catalysts. The defect formation energy is strongly influenced by the surface termination of the ceria particles and by the gold loading. Thus, choosing a sample with a CeO_2(110) surface termination and loading it with gold positively influences the activity. At the same time, we show that unloaded samples can be as active as gold-loaded ones, i.e., at higher temperatures it is possible to achieve similar CO conversion rates with the unloaded samples as with the gold loaded samples at lower temperatures. In this context, the barrier to

making surface oxygen available for CO_2 formation is thermally compensated. Thus, the main role of gold on the low-index surfaces is to allow milder reaction conditions. However, the role of gold as an active site loses importance at higher temperatures, as the bare support becomes more active, by thermal activation of lattice oxygen. In addition, we observe strong peroxide formation at the gold-loaded samples under reaction conditions (45 °C). To this end, we propose that peroxide formation may suppress CO adsorption and thus reaction, because of the higher adsorption energy of O_2 compared to CO (not subject to carbonate formation) and due to steric effects. Furthermore, the formation of carbonate species at lower temperatures may block active sites because of high adsorption energies of carbonates on CeO_2(100) and CeO_2(110). To conclude**,** our results show the potential of combining *operando* spectroscopies and DFT calculations to gain new insight into the facet-dependent reactivity behaviour of ceria-based gold catalysts for CO oxidation. In particular, the rods show stronger oxygen dynamics than the cubes regarding peroxide and oxygen defect formation. Furthermore, in contrast to the cubes, the rods can be re-oxidized after reaction conditions.

Acknowledgements

The DFT calculations were conducted on the Lichtenberg high performance computer of the TU Darmstadt. Jochen Rohrer and Karsten Albe are acknowledged for support with the VASP code. We thank Stefan Lauterbach and Hans-Joachim Kleebe for TEM measurements, Martin Brodrecht for BET measurements, and Karl Kopp for technical support as well as for XPS measurements.

Supporting Information

UV-vis, Raman, and XP spectra; reactivity data; results from theoretical calculations.

References and notes

1 M. Haruta, T. Kobayashi, H. Sano and N. Yamada, *Chem. Lett.*, 1987, **16**, 405–408.

2 S. Carrettin, P. Concepción, A. Corma, J. M. López Nieto and V. F. Puntes, *Angew. Chem. Int. Ed.*, 2004, **43**, 2538–2540.

3 A. Trovarelli and P. Fornasiero, *Catalysis by Ceria and Related Materials*, Imperial College Press, 2013, vol. 12.

4 Y. Ren, K. Tang, J. Wei, H. Yang, H. Wei and Y. Yang, *Energy Technol.*, 2018, **6**, 379–390.

5 T. Montini, M. Melchionna, M. Monai and P. Fornasiero, *Chem. Rev.*, 2016, **116**, 5987–6041.

6 T. Tabakova, F. Boccuzzi, M. Manzoli, J. W. Sobczak, V. Idakiev and D. Andreeva, *Appl. Catal. B Environ.*, 2004, **49**, 73–81.

7 H. Ha, S. Yoon, K. An and H. Y. Kim, *ACS Catal.*, 2018, **8**, 11491–11501.

8 Z. A. Qiao, Z. Wu and S. Dai, *ChemSusChem*, 2013, **6**, 1821–1833.

9 M. Ziemba, V. Ganduglia-Pirovano and C. Hess, *Faraday Discuss.*, , DOI:10.1039/C9FD00133F.

10 X.-L. Wang, X.-P. Fu, W.-W. Wang, C. Ma, R. Si and C.-J. Jia, *J. Phys. Chem. C*, 2019, **123**, 9001–9012.

11 M. Haruta, *Faraday Discuss.*, 2011, **152**, 11.

12 M. Flytzani-Stephanopoulos and B. C. Gates, *Annu. Rev. Chem. Biomol. Eng.*, 2012, **3**, 545–574.

13 Y.-G. Wang, D. Mei, V.-A. Glezakou, J. Li and R. Rousseau, *Nat. Commun.*, 2015, **6**, 6511.

14 J. Wang, H. Tan, S. Yu and K. Zhou, *ACS Catal.*, 2015, **5**, 2873–2881.

15 O. Bondarchuk, S. Shaikhutdinov and H.-J. Freund, *J. Phys. Chem. C*, 2019, **123**, 12376–12381.

16 J.-C. Liu, Y.-G. Wang and J. Li, *J. Am. Chem. Soc.*, 2017, **139**, 6190–6199.

17 M. Nolan, *J. Chem. Phys.*, 2009, **130**, 144702.

18 M. Nolan, V. S. Verdugo and H. Metiu, *Surf. Sci.*, 2008, **602**, 2734–2742.

19 H. Y. Kim and G. Henkelman, *J. Phys. Chem. Lett.*, 2012, **3**, 2194–2199.

20 A. Trovarelli and J. Llorca, *ACS Catal.*, 2017, **7**, 4716–4735.

21 M. Nolan, in *Catalysis by Materials with Well-Defined Structures*, Elsevier, 2015, pp. 159–192.

22 C. Schilling, M. V. Ganduglia-Pirovano and C. Hess, *J. Phys. Chem. Lett.*, 2018, **9**,

6593–6598.

23 Z. Wu, M. Li and S. H. Overbury, *J. Catal.*, 2012, **285**, 61–73.

24 M. Nolan, S. C. Parker and G. W. Watson, *Surf. Sci.*, 2006, **600**, 175–178.

25 M. Nolan and G. W. Watson, *J. Phys. Chem. B*, 2006, **110**, 16600–16606.

26 N. M. Galea, D. O. Scanlon, B. J. Morgan and G. W. Watson, *Mol. Simul.*, 2009, **35**, 577–583.

27 H. Y. Kim and G. Henkelman, *J. Phys. Chem. Lett.*, 2013, **4**, 216–221.

28 Q. Wu, F. Zhang, P. Xiao, H. Tao, X. Wang, Z. Hu and Y. Lü, *J. Phys. Chem. C*, 2008, **112**, 17076–17080.

29 H.-X. Mai, L.-D. Sun, Y.-W. Zhang, R. Si, W. Feng, H.-P. Zhang, H.-C. Liu and C.-H. Yan, *J. Phys. Chem. B*, 2005, **109**, 24380–24385.

30 S. Brunauer, P. H. Emmett and E. Teller, *J. Am. Chem. Soc.*, 1938, **60**, 309–319.

31 TEM analysis confirms that the morphology and size of the particles does not change during the gold loading and exposure to water-gas shift conditions, which are more drastically than CO oxidation conditions.

32 A. Laachir, V. Perrichon, A. Badri, J. Lamotte, E. Catherine, J. C. Lavalley, J. El Fallah, L. Hilaire, F. Le Normand, E. Quéméré, G. N. Sauvion and O. Touret, *J. Chem. Soc. Faraday Trans.*, 1991, **87**, 1601–1609.

33 D. A. Shirley, *Phys. Rev. B*, 1972, **5**, 4709–4714.

34 C. T. Nottbohm and C. Hess, *Catal. Commun.*, 2012, **22**, 39–42.

35 C. Schilling and C. Hess, *J. Phys. Chem. C*, 2018, **122**, 2909–2917.

36 C. Schilling and C. Hess, *ACS Catal.*, 2019, **9**, 1159–1171.

37 C. Schilling, A. Hofmann, C. Hess and M. V. Ganduglia-Pirovano, *J. Phys. Chem. C*, 2017, **121**, 20834–20849.

38 S. L. Dudarev, G. A. Botton, S. Y. Savrasov, C. J. Humphreys and A. P. Sutton, *Phys. Rev. B*, 1998, **57**, 1505–1509.

39 J. P. Perdew, K. Burke and M. Ernzerhof, *Phys. Rev. Lett.*, 1996, **77**, 3865–3868.

40 H. J. Monkhorst and J. D. Pack, *Phys. Rev. B*, 1976, **13**, 5188–5192.

41 M. Nolan, *J. Chem. Phys.*, 2012, **136**, 134703.

42 A. Chutia, D. J. Willock and C. R. A. Catlow, *Faraday Discuss.*, 2018, **208**, 123–145.

43 K.-J. Zhu, Y.-J. Yang, J.-J. Lang, B.-T. Teng, F.-M. Wu, S.-Y. Du and X.-D. Wen, *Appl. Surf. Sci.*, 2016, **387**, 557–568.

44 S. Fabris, G. Vicario, G. Balducci, S. De Gironcoli and S. Baroni, *J. Phys. Chem. B*, 2005, **109**, 22860–22867.

45 C. Zhang, A. Michaelides and S. J. Jenkins, *Phys. Chem. Chem. Phys.*, 2011, **13**, 22–33.

46 M. F. Camellone and S. Fabris, *J. Am. Chem. Soc.*, 2009, **131**, 10473–10483.

47 C. Zhang, A. Michaelides, D. A. King and S. J. Jenkins, *J. Phys. Chem. C*, 2009, **113**, 6411–6417.

48 J. Moulder, W. Stickle, P. Sobol and K. Bomben, *Handbook of X-ray Photoelectron Spectroscopy*, Physical Electronics, Inc., 1995.

49 C. W. M. Castleton, J. Kullgren and K. Hermansson, *J. Chem. Phys.*, 2007, **127**, 244704.

50 G. Ranga Rao and H. R. Sahu, *J. Chem. Sci.*, 2001, **113**, 651–658.

51 G. C. Allen, M. B. Wood and J. M. Dyke, *J. Inorg. Nucl. Chem.*, 1973, **35**, 2311–2318.

52 J. A. Hernández, S. A. Gómez, T. A. Zepeda, J. C. Fierro-González and G. A. Fuentes, *ACS Catal.*, 2015, **5**, 4003–4012.

53 A. Bensalem, J. C. Muller and F. Bozon-Verduraz, *J. Chem. Soc., Faraday Trans.*, 1992, **88**, 153–154.

54 E. Ruiz-Trejo, *J. Phys. Chem. Solids*, 2013, **74**, 605–610.

55 W. Song and E. J. M. Hensen, *J. Phys. Chem. C*, 2013, **117**, 7721–7726.

56 V. V. Pushkarev, V. I. Kovalchuk and J. L. D'Itri, *J. Phys. Chem. B*, 2004, **108**, 5341–5348.

57 S. Agarwal, L. Lefferts and B. L. Mojet, *ChemCatChem*, 2013, **5**, 479–489.

58 C. Wang, X.-K. Gu, H. Yan, Y. Lin, J. Li, D. Liu, W.-X. Li and J. Lu, *ACS Catal.*, 2017, **7**, 887–891.

59 C. Yang, X. Yu, S. Heißler, P. G. Weidler, A. Nefedov, Y. Wang, C. Wöll, T. Kropp, J. Paier and J. Sauer, *Angew. Chem. Int. Ed.*, 2017, **56**, 16399–16404.

60 Z. V. Popović, Z. Dohčević-Mitrović, M. J. Konstantinović and M. Šćepanović, *J. Raman Spectrosc.*, 2007, **38**, 750–755.

61 Z. Dohčević-Mitrović, Z. V. Popović and M. Šćepanović, *Acta Phys. Pol. A*, 2009, **116**, 36–41.

62 C. Schilling, M. Ziemba, C. Hess and M. V. Ganduglia-Pirovano, *J. Catal.*, 2020, **383**, 264–272.

63 M. Lohrenscheit and C. Hess, *ChemCatChem*, 2016, **8**, 523–526.

64 H. Y. Kim, H. M. Lee and G. Henkelman, *J. Am. Chem. Soc.*, 2012, **134**, 1560–1570.

65 W. Song and E. J. M. Hensen, *Catal. Sci. Technol.*, 2013, **3**, 3020.

66 B. Liu, W. Li, W. Song and J. Liu, *Phys. Chem. Chem. Phys.*, 2018, **20**, 16045–16059.

67 M. Huang and S. Fabris, *J. Phys. Chem. C*, 2008, **112**, 8643–8648.

68 C. Schilling and C. Hess, *Top. Catal.*, 2017, **60**, 131–140.

69 S. Agarwal, L. Lefferts, B. L. Mojet, D. A. J. M. Ligthart, E. J. M. Hensen, D. R. G. Mitchell, W. J. Erasmus, B. G. Anderson, E. J. Olivier, J. H. Neethling and A. K. Datye, *ChemSusChem*, 2013, **6**, 1898–1906.